

Accuracy and limitations of the bond polarizability model in modeling of Raman scattering from molecular dynamics simulations

Atanu Paul,¹ Maya Rubenstein,¹ Anthony Ruffino,² Stefan Masiuk,³ Jonathan Spanier,^{2,3} and Ilya Grinberg¹

¹*Department of Chemistry, Bar-Ilan University, Ramat Gan 5290002, Israel*

²*Department of Physics, Drexel University, Philadelphia, Pennsylvania 19104, USA*

³*Department of Mechanical Engineering and Mechanics, Drexel University, Philadelphia, Pennsylvania 19104, USA*

(*ilya.grinberg@biu.ac.il)

Calculation of Raman scattering from molecular dynamics (MD) simulations requires accurate modeling of the evolution of the electronic polarizability of the system along its MD trajectory. For large systems, this necessitates the use of atomistic models to represent the dependence of electronic polarizability on atomic coordinates. The bond polarizability model (BPM) is the simplest such model and has been used for modeling the Raman spectra of molecular systems but has not been applied to solid-state systems. Here, we systematically investigate the accuracy and limitations of the BPM parameterized from density functional theory (DFT) results for a series of simple molecules such as CO₂, SO₂, H₂S, H₂O, NH₃, and CH₄, the more complex CH₂O, CH₃OH and CH₃CH₂OH and thiophene molecules and the BaTiO₃ and CsPbBr₃ perovskite solids. We find that BPM can reliably reproduce the overall features of the Raman spectra such as shifts of peak positions. However, with the exception of highly symmetric systems, the assumption of non-interacting bonds limits the quantitative accuracy of the BPM; this assumption also leads to qualitatively inaccurate polarizability evolution and Raman spectra for systems where large deviations from the ground state structure are present.

I. INTRODUCTION

Spectroscopy is as a powerful tool that has been widely applied to various inorganic and organic systems to obtain the characteristic vibrations and other related properties^{1,2}. The application of molecular dynamics (MD) simulations for the interpretation of infrared (IR) spectra has provided a powerful method for detailed understanding of experimental IR spectroscopy results, significantly enhancing the value provided by IR spectra^{3,4}. By contrast, obtaining a similar level of microscopic insight from Raman scattering with the help of MD simulations has not been possible due to the difficulties in the evaluation of the electronic polarizability trajectory.

The Raman spectrum of a system owing to its lattice dynamics can be calculated from the changes in the electronic polarizability of the system due to its atomic (or ionic) vibrations. Therefore, to model the Raman spectra using MD simulations, electronic polarizability along the trajectory of the system dynamics must be calculated, and then the Raman spectrum can be obtained from the auto-correlation function of the time-dependent electronic polarizability trajectory⁵⁻⁷. Electronic polarizability is an observable related to the electronic response of the system to the perturbation by an applied electric field, and ideally should be obtained by quantum-mechanical (QM) calculations^{8,9}. However, such QM calculation of electronic polarizability at each time step has a very high computational cost. While atomistic models using neural networks for estimation of electronic polarizability trajectories have been developed, due to their complexity they still have a high computational cost, albeit much smaller one than that of direct QM calculations, and require large amount of QM data for model training¹⁰⁻¹³. Therefore, modeling the electronic polarizability dynamics for large systems is still

challenging.

Among the atomistic approaches for electronic polarizability evaluation, the bond polarizability model (BPM)¹⁴⁻¹⁶, is the simplest and the most computationally efficient. This simple model is based on the assumption that the total polarizability of the system is the sum of the polarizability contributions of the individual bonds. The model also assumes that the polarizability contribution of each bond is a function of the length of that bond only, i.e. independent bond approximation. Despite these simplistic assumptions, BPM has been applied and found to be accurate for obtaining Raman spectra in various systems¹⁷⁻²⁰. However, it was also found to be inaccurate for some molecular and solid state systems^{21,22}. Therefore, it is important to analyze the BPM as the simplest possible electronic polarizability model to systematically evaluate the limits of its applicability to the study of molecular and solid-state systems and to provide a baseline reference for the development of more sophisticated electronic polarizability models.

In this paper, we first applied the BPM to simple molecules such as the linear molecule CO₂, and several two-element non-linear molecules SO₂, H₂S, H₂O, NH₃ and CH₄ with different bond angles; these molecules are used as model systems to understand the effect of bond angles on the BPM accuracy. We then examined the more complicated multielement CH₂O and CH₃OH and CH₃CH₂OH and thiophene molecules to understand the impact of various degrees of freedom of molecular structures on larger molecules in the application of BPM. Finally, we applied the BPM to perovskites as model solid state systems due to their broad range of functional properties and rich physics. In particular, we focused on the classic oxide ferroelectric (FE) BaTiO₃ (BTO) and halide perovskite CsPbBr₃ (CPB). For all of these systems, we compare the

BPM results for the polarizability and Raman spectra with those obtained by direct density functional theory (DFT) calculations for small systems. Our results show that despite its simplicity, BPM can be useful and accurate for capturing the overall features of the Raman spectra; however, BPM fails to reproduce fine polarizability changes and some features of Raman spectra when encountering strong asymmetric vibrations and strong anharmonicity. Our results thus demonstrate the limits of accuracy of the BPM approach, providing guidance for modeling of Raman spectroscopy results and also providing a baseline for the development of more accurate atomistic and neural network models of polarizability dynamics.

II. METHODS

A. Bond Polarizability Model and computational methods

In this work, the total polarizability tensor (α_{ij}) is defined as

$$\alpha_{ij} = \frac{1}{\Omega} \sum_n \alpha_{ij}^n$$

where Ω is the volume and α_{ij}^n is the polarizability tensor for the n^{th} bond. Furthermore, α_{ij}^n is defined as

$$\alpha_{ij}^n = \frac{1}{3}(\alpha_l + 2\alpha_p)\delta_{ij} + (\alpha_l - \alpha_p)\left(\frac{R_i R_j}{R^2} - \frac{1}{3}\delta_{ij}\right)$$

where i, j denote x, y or z axes. \mathbf{R} is the vector between two atoms forming the n^{th} bond, and α_l and α_p are the longitudinal and perpendicular bond polarizabilities, respectively for a particular bond type. According to BPM, these parameters are functions of the bond length R only. Therefore, the bond polarizabilities can be expanded in a Taylor series with respect to the bond length around the equilibrium structure denoted by superscript 0, as given by

$$\alpha_t = \alpha_t^0 + \alpha_t^1 \cdot (R - R^0) + \alpha_t^2 \cdot (R - R^0)^2 + \dots$$

where α_t is either longitudinal ($t = l$) or perpendicular ($t = p$) component of the bond polarizability.

In order to extract the unknown parameters of the BPM, we calculated polarizability trajectory using density functional perturbation theory (DFPT)²³ as implemented in Quantum ESPRESSO code²⁴. For all of the systems considered here, *ab initio* molecular dynamics were also performed using Quantum ESPRESSO. The Perdew-Burke-Ernzerhof exchange-correlation functional for solids (PBEsol) was employed for all systems²⁵. All the unknown parameters in the BPM then were extracted by minimizing the difference between the model results and the training data set along the DFPT-calculated polarizability trajectory.

For CO_2 , SO_2 , H_2S , H_2O and NH_3 , *ab initio* molecular dynamics simulations were performed at 300 K. First, we calculated polarizability trajectory directly using DFT for 30, 24, 25 and 24 ps with a time step of 0.0015 ps for the CO_2 , SO_2 , H_2S , H_2O and NH_3 molecules, respectively. However,

due to computational cost, we considered the DFT-calculated polarizability trajectory for 23, 24, 23, 20 and 20 ps with a time step of 0.0058, 0.0058, 0.0058, 0.0072 and 0.0072 ps in case of CH_4 , CH_2O , CH_3OH , $\text{CH}_3\text{CH}_2\text{OH}$ and thiophene, respectively. We then extracted the BPM parameters for 1st- and 2nd-order models using the DFT-calculated polarizability trajectory data. For BTO and CPB, we found that the polarizability is dominated by the contributions from the motions of the TiO_6 and PbBr_6 octahedra (see Supplementary Material (SM)). Therefore, BPM parameters are extracted after fitting to the Ti-O and Pb-Br bonds, respectively, for these systems. We considered a 10-atom unit cell and performed molecular dynamics for 30 ps with a time step of 0.0015 ps while keeping the cell volume fixed at four temperatures of 300 K, 600 K, 800 K and 1000 K, respectively. For the DFT-calculated polarizability trajectory, we considered the full trajectory of 30 ps with a time step of 0.073 ps. The DFT-calculated polarizability trajectories for all temperatures were used for the extraction of the BPM parameters.

For classical molecular dynamics of BTO, we used a $10 \times 10 \times 10$ supercell for 300 ps with a time step of 0.001 ps with the LAMMPS code²⁶ using the bond-valence model atomistic potential (BVMD)²⁷. Then, BPM parameters as extracted from the polarizability calculations for the 10-atom unit cell were used to calculate the Raman spectra of bulk and thin film of BTO for various temperatures.

B. Experimental details

Raman scattering was collected in the backscattering configuration ($Z(X,X)\bar{Z}$, $X \parallel (100)$), with a 5 mW 385 nm laser excitation source focused to a surface intensity of 1 W/cm². Light was dispersed by a triple spectrometer operated in a double-dispersive single-subtractive mode (Horiba Jobin-Yvon, model T64000), and collected using a thermoelectrically-cooled CCD (Andor). The (001)-oriented BaTiO_3 bulk single crystal was grown by top seeded solution growth (MTI Corp.).

Raman spectra were collected between 123 K and 423 K at 5 K intervals, and each individual spectrum is the average of 3 acquisitions for 10 s each. Experimental observations of abrupt structural phase transitions at 183 K (rhombohedral (R) to orthorhombic (O)), 278 K (O to tetragonal (T)), and 393 K (T to cubic (C)) are in agreement with the BTO results reported in the literature²⁸. Additionally, the intensity of the collapsing soft mode (160 cm⁻¹ in the R-phase, and the broad feature at 35 cm⁻¹ in the O-phase) are an indication of structural homogeneity and a low population of domain walls, showing that these are effectively single-domain measurements²⁹.

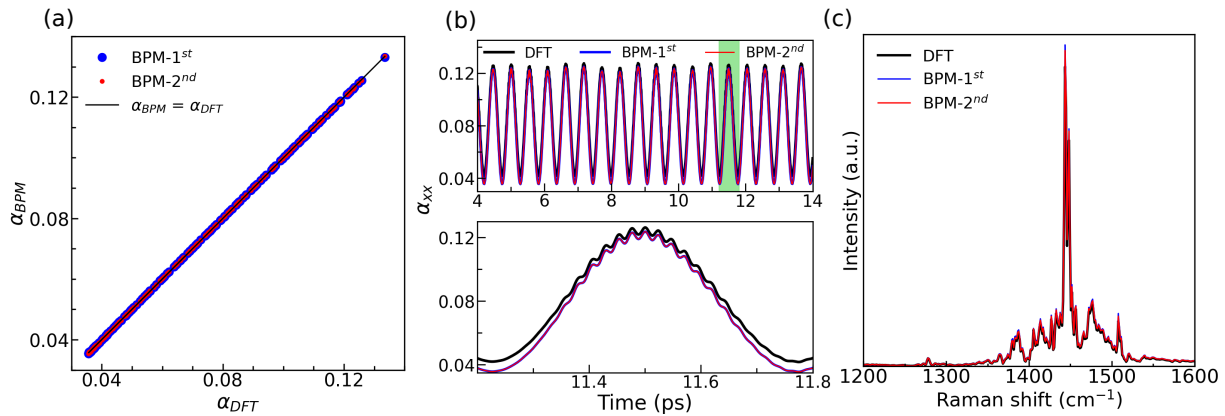


FIG. 1. (Color online) CO₂: (a) The xx component of α_{BPM} (1st and 2nd order are shown by blue and red circles, respectively) vs α_{DFT} . The linear fit of BPM-2nd order data is shown by the black line. (b) Top panel: Comparison of time-dependent trajectory of α_{xx} . Bottom panel: Magnified view of the region in first panel marked in filled green color. (c) Raman spectra from DFT (black), BPM-1st (blue) and BPM-2nd (red).

III. RESULTS AND DISCUSSION

A. Linear CO₂ molecule

Fig. 1 (a) compares the polarizabilities calculated using BPM and DFT along the polarizability trajectory of the xx component at 300 K for CO₂. Both 1st- and 2nd-order BPM reproduce the DFT polarizability very accurately (see the linear fit of the 2nd order BPM data). We also compare polarizability trajectory (α_{xx}) as calculated from DFT and BPM (1st and 2nd) in Fig. 1 (b). The top panel of Fig. 1 (b), which presents the overall polarizability trajectory, shows perfect agreement between the overall trajectories from BPM and DFT, corresponding to low-frequency vibrations. The bottom panel of Fig. 1 (b), which presents a magnified view of a small region of the trajectory also shows good agreement between the model and DFT results for the high-frequency polarizability oscillations. This demonstrates the accuracy of BPM on simple linear molecule such as CO₂. Therefore, it is expected that the Raman spectrum calculated using BPM will capture the main peaks of the DFT Raman spectrum. Fig. 1 (c) shows the perfect overlap of peak positions and intensities of the Raman spectra obtained by these two methods. These results show that the polarizability fluctuations are well-reproduced by the BPM.

B. Nonlinear molecules

Then, we considered the SO₂, H₂S, H₂O, NH₃ and CH₄ nonlinear molecules in order to examine the effect of angular geometry on the BPM accuracy. Fig. 2 (a) compares the calculated values of the the xx component of α_{BPM} for 1st and 2nd order BPM with α_{DFT} for SO₂. The scatter of the data around the $y = x$ line ($\alpha_{BPM} = \alpha_{DFT}$) shows that the 1st-order BPM cannot fully capture the DFT values. These results are not improved even after the application of the 2nd-order BPM.

However, an overall linear dependence of α_{BPM} plotted versus α_{DFT} is observed (the equation of the linear fit of the 2nd order BPM α values plotted versus DFT α values is $\alpha_{BPM} = 0.01 + 0.924^* \alpha_{DFT}$) with an increase of the deviation of the value of α_{BPM} from α_{DFT} when going from larger to smaller values of α_{DFT} , forming a triangular-like data distribution. We also plotted the polarizability trajectories at 300 K of SO₂ from these different methods in Fig. 2 (b). The gross features of the DFT trajectory are reproduced well by the 1st and 2nd order BPM. Even though the low-frequency (top panel of Fig. 2 (b)) and high-frequency (bottom panel of Fig. 2 (b)) polarizability fluctuations are well-captured by the BPM, the amplitude of the low- and high-frequency fluctuations from the BPM results shows some differences from the DFT results. These discrepancies are reflected in the calculated Raman spectra for the high-frequency region (see Fig. 2 (c)), where the spectral positions of the DFT-generated spectra are reproduced well by the BPM-generated spectra. However, unlike for CO₂, the peak intensities from BPM do not agree with the DFT results. Additionally, differences between the Raman intensities of the DFT and BPM spectra are also observed for the low-frequency peaks (see inset Fig. 2 (c)).

Next, we examined the BPM results for H₂S. Fig. 3 (a), presents the results for BPM-calculated α plotted versus DFT-calculated α for the xx component. Similar to SO₂, the 1st order α_{BPM} values show high scatter in comparison to α_{DFT} forming a triangular data distribution where the deviation of the BPM-generated α values from the DFT-generated α increases drastically while moving from higher to lower values of DFT-generated α . Inclusion of 2nd order in the BPM improves the results slightly so that only a small decrease in the size of the triangular data distribution is obtained. The inclusion of higher-order (3rd and 4th order) terms in the BPM did not eliminate this error, indicating that it is due to the lack of consideration of the effects of the H-S-H angle on the polarizability. The α_{xx} polarizability trajectories from different methods are shown in Fig. 3 (b), revealing poor agreement between the BPM- and DFT-calculated polarizability trajec-

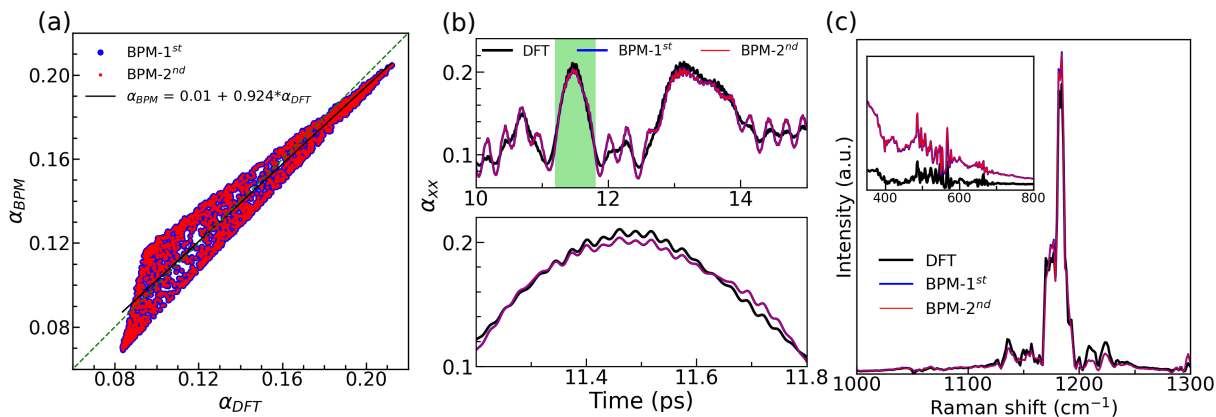


FIG. 2. (Color online) SO₂ (a) The xx component of α_{BPM} (1st and 2nd order are shown by blue and red circles, respectively) vs α_{DFT} . The linear fit of the BPM-2nd order data is shown by solid black line. The green dotted line represents $\alpha_{BPM} = \alpha_{DFT}$. (b) Top panel: Comparison of the trajectory of α_{xx} . Bottom panel: Magnified view of the region shaded in green in the first panel. (c) Raman spectra from DFT (black), BPM-1st (blue) and BPM-2nd (red) results. Inset shows the results in the lower-wavenumber region.

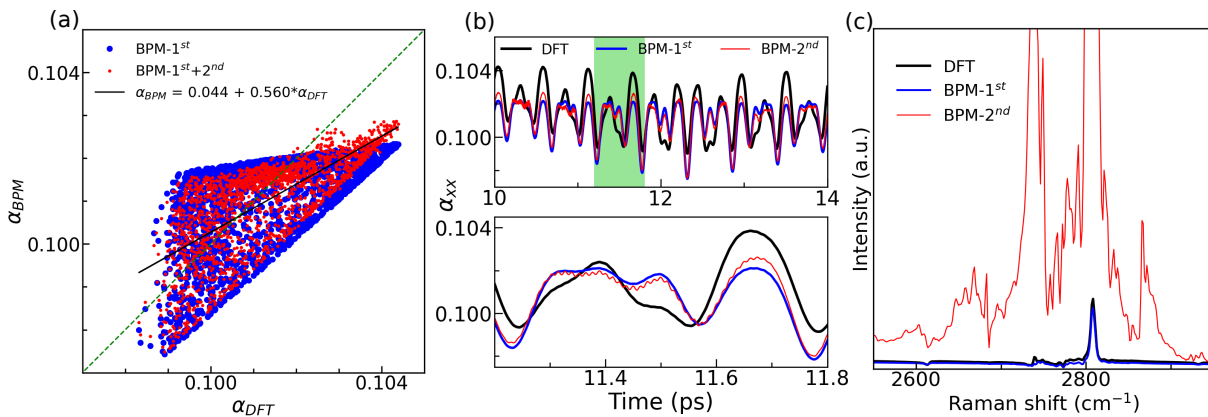


FIG. 3. (Color online) H₂S: (Color online) (a) The results for the xx component of α_{BPM} (1st and 2nd order BPM are shown by blue and red circles, respectively) plotted vs α_{DFT} . The linear fit of BPM-2nd order data is shown by the black line. The green dotted line represents $\alpha_{BPM} = \alpha_{DFT}$. (b) Top panel: Comparison of the trajectory of α_{xx} . Bottom panel: Magnified view of the region in the first panel shaded in green. (c) Raman spectra generated using DFT (black), BPM-1st (blue) and BPM-2nd (red).

ries. A small improvement by the 2nd-order model compared to the 1st-order model is observed for the overall variation of α_{xx} (Top panel of Fig. 3 (b)). However, a magnified view of the α_{xx} trajectories shows that the 2nd-order model trajectory exhibits much stronger high-frequency fluctuations compared to both the DFT or 1st-order model trajectories.

These much stronger high-frequency fluctuations lead to a dramatically higher Raman intensity for the high-frequency peaks predicted by the 2nd-order model compared to the DFT and 1st order model spectra (Fig. 3 (c)). Both BPM-1st and BPM-2nd order models predict peak positions similar to those of DFT in the high-frequency spectrum. However, comparison of the obtained peak intensities shows that the BPM-1st spectrum is closer to the DFT spectrum than the BPM-2nd spectrum. The unphysically high intensity of the high-frequency fluctuations in the BPM-2nd order model is likely due to the fact that the model parameterization procedure seeks to minimize the overall error; since the high-frequency oscillations are much weaker than the low-frequency oscillations,

an overestimation of high-frequency amplitude will be acceptable in the parameterization if it is balanced by better agreement with the overall trajectory. However, this will lead to unphysically high intensity in the physically relevant part of the spectrum.

We then examine the performance of BPM for H₂O, perhaps the most important molecule in chemistry and biology. Fig. 4 (a) shows α_{xx} calculated using BPM-1st and BPM-2nd for different H₂O geometries plotted versus the corresponding DFT α_{xx} values. Similar to other nonlinear molecules, a triangular data distribution is observed for both BPM-1st and BPM-2nd. However, unlike for H₂S, the inclusion of 2nd order does not improve the BPM results. The calculated slope (0.275) of the linear fit of the BPM-2nd vs DFT data is even worse than that for H₂S (0.560). We also plot the polarizability trajectories as calculated from BPM-1st, BPM-2nd and DFT methods in Fig. 4 (b). The low-frequency polarizability trajectory (see top panel of Fig. 4 (b)) is not well-captured by the BPM. However, the high-frequency oscillations of the polar-

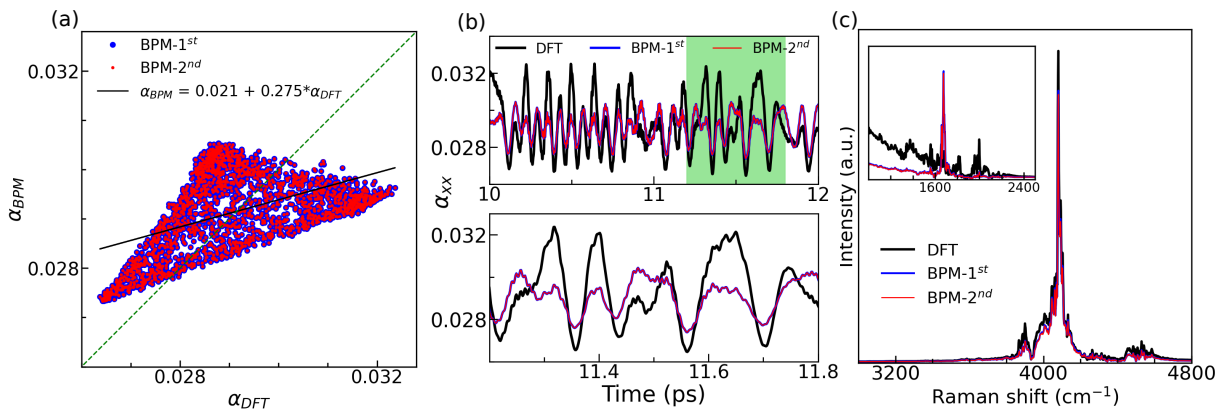


FIG. 4. (Color online) H₂O: (Color online) (a) The results for the xx component of α_{BPM} (1st and 2nd order BPM are shown by blue and red circles, respectively) plotted vs α_{DFT} . The linear fit of BPM-2nd order data is shown by the black line. The green dotted line represents $\alpha_{BPM} = \alpha_{DFT}$. (b) Top panel: Comparison of the trajectory of α_{xx} . Bottom panel: Magnified view of the region in the first panel shaded in green. (c) Raman spectra generated using DFT (black), BPM-1st (blue) and BPM-2nd (red).

izability trajectory are well-reproduced by BPM (see bottom panel of Fig. 4 (b)). This implies that the BPM-calculated Raman spectrum will be in good agreement with the DFT spectrum in the high-frequency region but not in the low-frequency region. The Raman spectra (Fig. 4 (c)) calculated from the polarizability trajectory show that the peak position in the high-frequency range is well-reproduced by the BPM-1st and BPM-2nd. However, a small disagreement between the peak intensities between BPM and DFT spectra is observed in this region. By contrast, the spectra in the low-frequency region (inset of Fig. 4 (c)) do not show good agreement with the DFT results.

Next, we consider NH₃ and CH₄ which are nonlinear molecules with multiple equal bond angles. While naively, one may expect the BPM polarizability to show stronger disagreement with DFT results for NH₃ compared to H₂O due to a greater number of bond angles, in contrast to the results for H₂S, H₂O and SO₂, the plot of BPM polarizability versus DFT polarizability shows a good linear trend Fig. 5 (a). The overall α_{xx} trajectory is also reproduced well (top panel of Fig. 5 (b)). However, a magnified view of the trajectory shows significant differences between the high-frequency α_{xx} oscillations predicted by BPM and those obtained by DFT calculations, with much larger amplitude of oscillations for the DFT trajectory (bottom panel of Fig. 5 (b)). Correspondingly, examination of the Raman spectra presented in Fig. 5 (c) shows that the high-frequency peaks of the DFT spectrum have much higher intensity than the corresponding BPM peaks. While BPM and DFT obtain the same frequencies for the peaks, the relative intensities of the peaks are somewhat different. Thus, similar to H₂S, H₂O and SO₂, BPM correctly reproduces the peak positions but does not accurately reproduce the fine features of the DFT spectra.

Next, examination of the CH₄ results in Fig. 6 reveals good agreement between BPM and DFT results with only a small deviation from $y = x$ line. A close examination of the polarizability trajectory and the Raman spectrum reveals small but noticeable differences. Thus, while accurate, the BPM for CH₄ does not show perfect agreement such as that found for

CO₂, indicating that the lack of a bond-angle-dependent term in the BPM does affect the accuracy of model polarizability, even though the effect is weak.

We now discuss the origin of the polarizability errors of the BPM in the angular molecules. The BPM is a Taylor expansion of the polarizability around the ground state structure, where rather than carrying out the Taylor expansion in terms of the Cartesian coordinates of the atoms, the Taylor expansion is carried out in terms of the deviations of the bond lengths from their ground state values. However, for tri-atomic molecules, in addition to the bond lengths, the bond angle can also affect the polarizability and a full Taylor expansion should involve angle-dependent terms such as $a_{\theta}\Delta\theta + b_{\theta}(\Delta\theta)^2 + \dots$ as well as cross-terms describing the interplay of the effects of the bond length and bond angle, such as $a_{r,\theta}\Delta\theta\Delta r + \dots$. Clearly, these terms are absent in the BPM that only takes into account the changes in the bond lengths and ignores the effect of the angle.

For a Taylor expansion, we expect that higher-order terms are weaker than the lower-order terms. Thus, the linear effect of the change in θ given by $a_{\theta}\Delta\theta$ is larger than the quadratic effect given by $b_{\theta}(\Delta\theta)^2$. In a tri-atomic angular molecule such as water, a vibration that changes the bond angle will change the polarizability by $a_{\theta}\Delta\theta + b_{\theta}\Delta\theta^2 + a_{r,\theta}\Delta\theta\Delta r$. For the water molecule with only one bond angle, any motion of the O-H bonds that changes the bond angle is uncompensated by an equal and opposite change in a different bond angle, so that the error is of the order $a_{\theta}\Delta\theta + b_{\theta}(\Delta\theta)^2 + a_{r,\theta}\Delta\theta\Delta r$. However, for a molecule such as CH₄, any movement of the C-H bond that leads to a change in the bond angle makes one bond angle smaller and another bond angle greater. This leads to the cancellation of the first-order effects of both the θ and the θr terms, so that the error is given by $b_{\theta}(\Delta\theta)^2$ only and is much smaller than that for water. For NH₃, the size of the error depends on the direction of vibration. For a vibration by an N-H bond toward another N-H bonds, the linear effects will be canceled out and the error due to ignoring the angular effect will be only second order in $\Delta\theta$ and small. How-

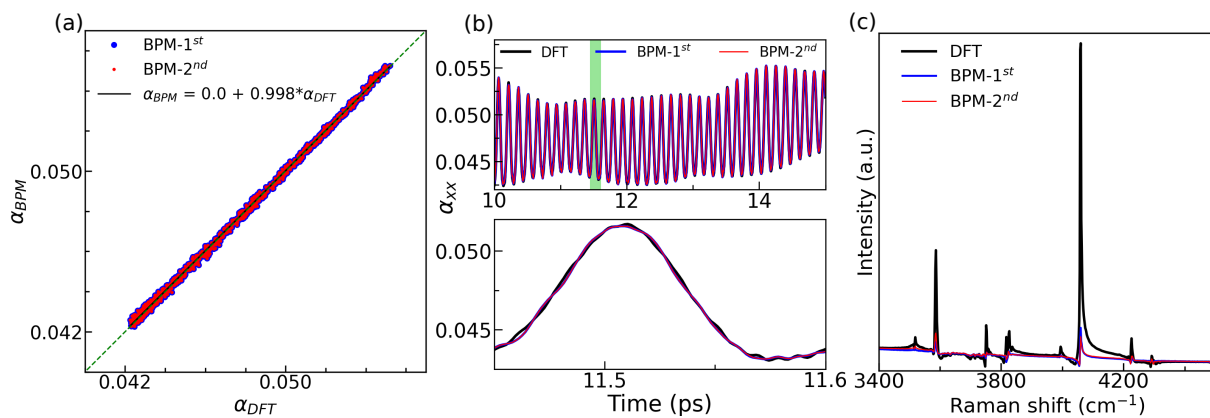


FIG. 5. (Color online) NH₃: (Color online) (a) The results for the xx component of α_{BPM} (1st and 2nd order BPM are shown by blue and red circles, respectively) plotted vs α_{DFT} . The linear fit of BPM-2nd order data is shown by the black line. The green dotted line represents $\alpha_{BPM} = \alpha_{DFT}$. (b) Top panel: Comparison of the trajectory of α_{xx} . Bottom Panel: Magnified view of the region in the top panel shaded in green. (c) Raman spectra generated using DFT (black), BPM-1st (blue) and BPM-2nd (red).

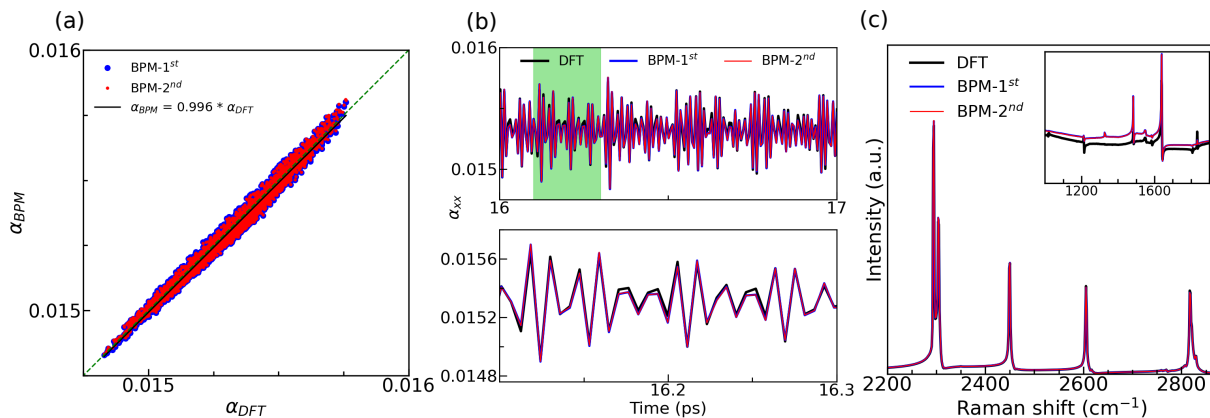


FIG. 6. (Color online) CH₄: (Color online) (a) The results for the xx component of α_{BPM} (1st and 2nd order BPM are shown by blue and red circles, respectively) plotted vs α_{DFT} . The linear fit of BPM-2nd order data is shown by the black line. The green dotted line represents $\alpha_{BPM} = \alpha_{DFT}$. (b) Top panel: Comparison of the trajectory of α_{xx} . Bottom panel: Magnified view of the region in the first panel shaded in green. (c) Raman spectra generated using DFT (black), BPM-1st (blue) and BPM-2nd (red).

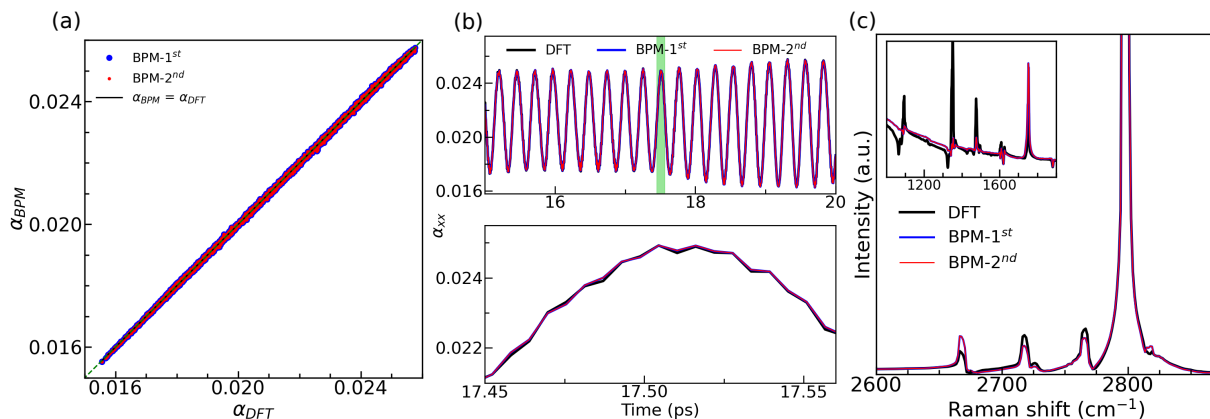


FIG. 7. (Color online) CH₂O: (Color online) (a) The results for the xx component of α_{BPM} (1st and 2nd order BPM are shown by blue and red circles, respectively) plotted vs α_{DFT} . The linear fit of BPM-2nd order data is shown by the black line. The green dotted line represents $\alpha_{BPM} = \alpha_{DFT}$. (b) Top panel: Comparison of the trajectory of α_{xx} . Bottom panel: Magnified view of the region in the first panel shaded in green. (c) Raman spectra generated using DFT (black), BPM-1st (blue) and BPM-2nd (red).

ever for a vibration by an N-H bond toward the N lone pair, the linear angular effect will be present and the error will be large. Therefore, we observe very larger deviation of BPM results for polarizability in the α_{BPM} vs α_{DFT} plot for angular tri-atomic molecules H_2O , H_2S and SO_2 , a much smaller deviation for NH_3 and an even smaller deviation for CH_4 .

To further test the performance of BPM, we examine the more complicated tri-element molecules CH_2O (see Fig. 7) and CH_3OH (see Fig. 8). We find that despite the strong asymmetry of CH_2O , BPM shows small deviations from the DFT results. This is likely due to the high stiffness of the 120° H-C-O and the H-C-H angles that only allow small vibrations (considerably smaller than those for water) and therefore lead to only small deviations of BPM polarizability from the DFT polarizability even in the presence of error linear in θ . For CH_3OH , we find significant differences between BPM and DFT polarizability values, due to the larger fluctuations of the C-O-H bond angle for which the terms linear in θ are not canceled out. These results suggest that BPM will be accurate in the case where linear dependence of the polarizability on the bond angle is either zero due to the presence of multiple bonds such that the bond motion makes one bond angle greater and the other bond angle smaller, or is small due to the stiff double bonds. On the other hand, for highly asymmetric molecules with single bonds, and in particular for O atoms where only a single bond angle centered at O is possible, BPM errors due to ignoring the effect of θ will be significant. Comparison of the BPM results for polarizability and Raman spectra of thiophene (C_4H_4S) and CH_3CH_2OH with the corresponding DFT results confirm the above conclusions. For the aromatic thiophene molecule, small errors are obtained for the BPM polarizability results as shown in Figs. 9, with good agreement obtained for the Raman spectra except for the peak at 1450 cm^{-1} . This is due to the stiffness of the aromatic structure with 120° bond angles, similar to CH_2O . For CH_3CH_2OH , the agreement between the BPM and DFT polarizability values is similar to that for CH_3OH (see Figs. 10) and the Raman spectrum shows a similar poor agreement with the DFT spectrum for the $1200\text{-}1600\text{ cm}^{-1}$ region. These results suggest that spectral features related to asymmetric bonds will be reproduced relatively poorly by BPM for large molecule, even while the overall spectrum will show good agreement with DFT results due to the dominance of the functional groups for which the BPM model performs well (e.g. CH_3 and CH_2 in ethanol).

C. Perovskites

Multicenter bonding is important for solid-state materials and we therefore examine two perovskites, the classic ferroelectric BTO and the CPB halide perovskite, which are representative materials of the important oxide and halide perovskites in order to understand the effectiveness of the BPM for representing solid-state polarizability and Raman spectra. The perovskite structure enables a variety of different distortions that provide a good test of atomistic polarizability models. For example, BTO can assume four different phases

generated by different directions of average Ti displacements from the center of the O_6 octahedra that show different Raman spectra. Additionally, the presence of vibrational modes related to O_6 rotations also contributes to the Raman spectra of BTO. The soft bonds and strong distortions of CPB make it a particularly stringent test case for atomistic polarizability models²².

Fig. 11 (a) plots the α_{xx} values for both 1^{st} and 2^{nd} order BPM versus the DFT-calculated polarizability for ten-atom supercell of BTO at 300 K. It is observed that the BPM- 1^{st} order completely fails to reproduce the DFT-calculated polarizability data, whereas the inclusion of 2^{nd} order term in the BPM strongly improves the model predictions. For example, the slope of the line fit to the BPM-2 data plotted versus DFT data is 0.874, which is relatively close to the $\alpha_{BPM} = \alpha_{DFT}$ straight line. Nevertheless, large scatter is observed in the plot of DFT versus BPM- 2^{nd} polarizability. Inclusion of higher-order dependence of bond polarizability on bond length does not strongly improve the agreement of BPM with DFT (see SM), suggesting that the BPM error is due to the fundamental approximation of independent bond contributions to the polarizability of the BPM.

We then compare the polarizability trajectories (α_{xx} , α_{yy} , α_{zz}) calculated from BPM (1^{st} and 2^{nd}) and DFT methods as shown in Fig. 11 (b). The improvement of BPM results can be observed clearly after the inclusion of BPM- 2^{nd} order, which reproduces the overall trajectory well but shows local deviations from the DFT values. Here, we only compare the low-frequency region due to the large time step used to evaluate the polarizability trajectory.

The Raman spectra calculated using the polarizability trajectory with large time steps are shown in Fig. 11 (c). The BPM- 2^{nd} spectrum reproduces all of the peaks of the DFT spectrum, but shows strong differences in intensity for four peaks (at 110, 130, 170 and 215 cm^{-1}), indicating that BPM- 2^{nd} cannot reliably reproduce the lineshapes of the peaks in the Raman spectrum.

We then applied the same BPM parameters for the structures obtained in the DFT MD simulation of BTO performed at 1000 K in order to check the applicability of the BPM parameters at higher temperatures. Fig. 12 (a) shows the comparison of the BPM-calculated polarizability with the DFT-calculated polarizability. Similar to the 300 K results (Fig. 11 (a)), the BPM- 1^{st} order fail to reproduce the DFT-results. However, the BPM- 2^{nd} improved the value of polarizability so that the data points are more aligned along the $\alpha_{BPM} = \alpha_{DFT}$ straight line. The scatter of the data is greater than that for 300 K, most likely due to the more anharmonic vibrations, greater impact of the changes in the Ti-O-Ti and O-Ti-O bond angles, and greater coupling between the bonds. This can also be seen by comparing the calculated slope from the linear fitting, where the calculated value of the slopes are 0.866 and 0.778 at 300 K and 1000 K, respectively.

The direct comparison of the polarizability trajectories at 1000 K is shown in Fig. 12 (b). Similar to the results for the simulation at 300 K, the BPM- 2^{nd} captures the overall fluctuation of the polarizability very well. These results are also reflected in the calculated Raman spectra plot for the low-

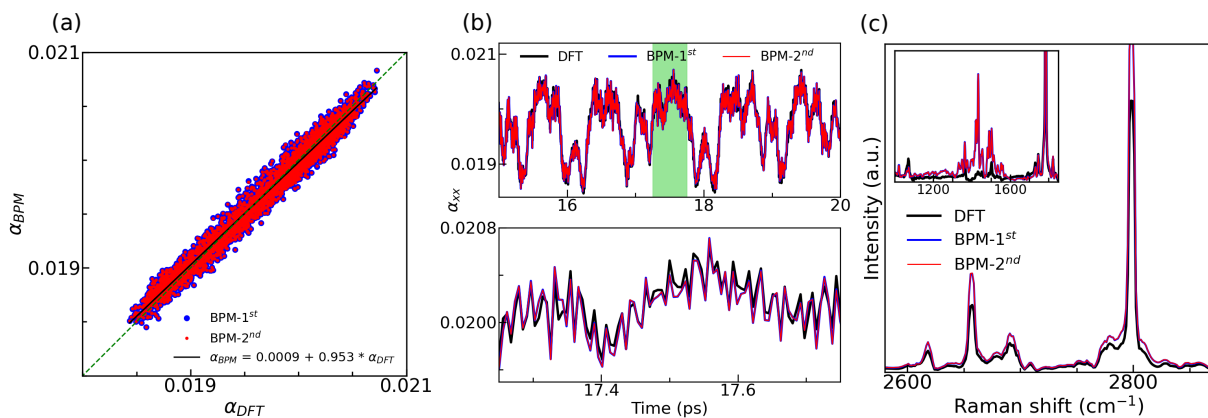


FIG. 8. (Color online) CH₃OH: (Color online) (a) The results for the xx component of α_{BPM} (1st and 2nd order BPM are shown by blue and red circles, respectively) plotted vs α_{DFT} . The linear fit of BPM-2nd order data is shown by the black line. The green dotted line represents $\alpha_{BPM} = \alpha_{DFT}$. (b) Top panel: Comparison of the trajectory of α_{xx} . Bottom panel: Magnified view of the region in the first panel shaded in green. (c) Raman spectra generated using DFT (black), BPM-1st (blue) and BPM-2nd (red).

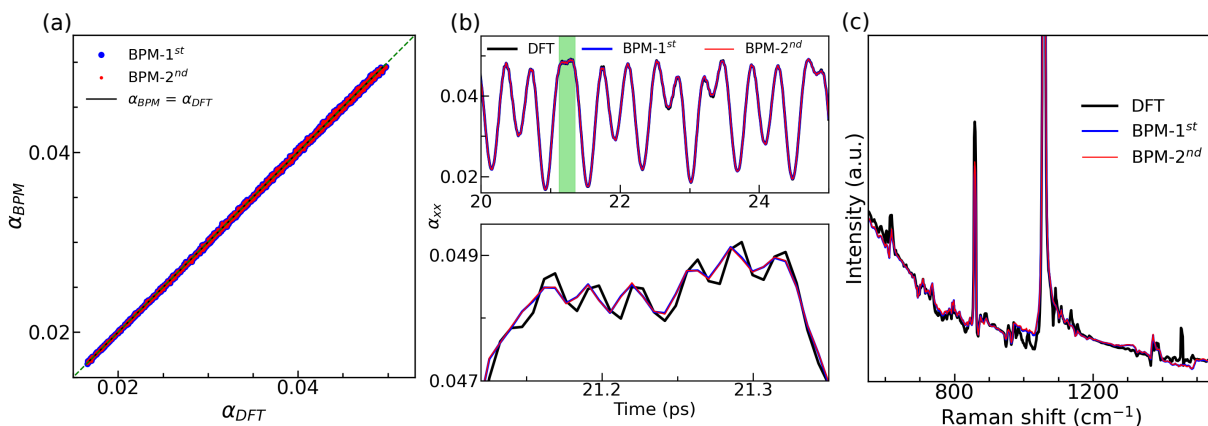


FIG. 9. (Color online) Thiophene: (Color online) (a) The results for the xx component of α_{BPM} (1st and 2nd order BPM are shown by blue and red circles, respectively) plotted vs α_{DFT} . The linear fit of BPM-2nd order data is shown by the black line. The green dotted line represents $\alpha_{BPM} = \alpha_{DFT}$. (b) Top panel: comparison of the trajectory of α_{xx} . Bottom panel: Magnified view of the region in the first panel shaded in green. (c) Raman spectra generated using DFT (black), BPM-1st (blue) and BPM-2nd (red).

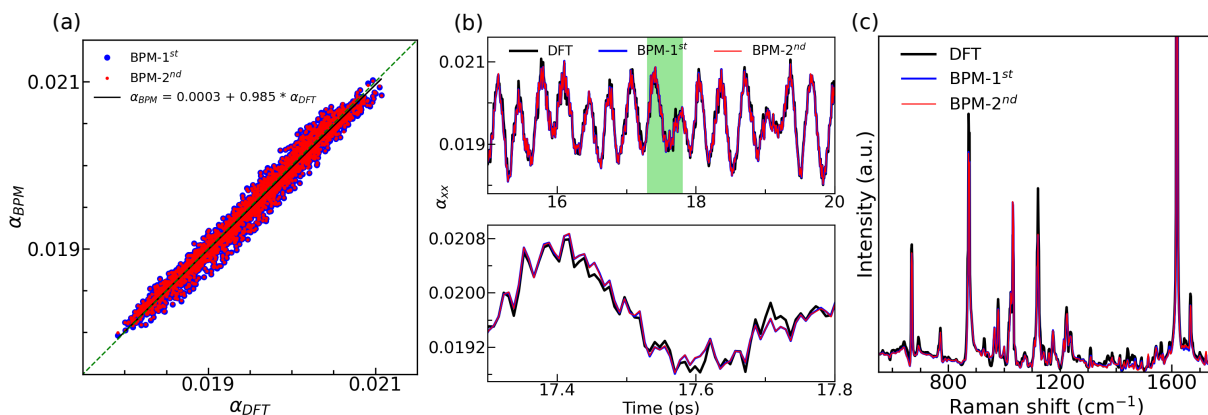


FIG. 10. (Color online) CH₃CH₂OH: (Color online) (a) The results for the xx component of α_{BPM} (1st and 2nd order BPM are shown by blue and red circles, respectively) plotted vs α_{DFT} . The linear fit of BPM-2nd order data is shown by the black line. The green dotted line represents $\alpha_{BPM} = \alpha_{DFT}$. (b) Top panel: Comparison of the trajectory of α_{xx} . Bottom panel: Magnified view of the region in the first panel shaded in green. (c) Raman spectra generated using DFT (black), BPM-1st (blue) and BPM-2nd (red).

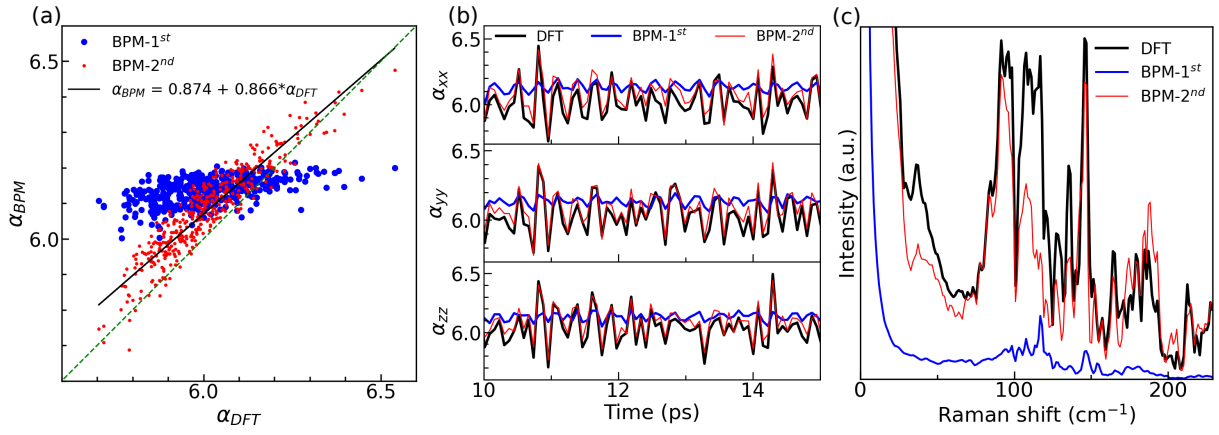


FIG. 11. (Color online) BaTiO₃ at 300 K: (Color online) (a) The results for the xx component of α_{BPM} (1st and 2nd order BPM are shown by blue and red circles, respectively) plotted vs α_{DFT} . The linear fit of BPM-2nd order data is shown by the black line. The green dotted line represents $\alpha_{BPM} = \alpha_{DFT}$. (b) Comparison of the trajectory of α_{xx} (top panel), α_{yy} (middle panel) and α_{zz} (bottom panel) calculated from DFT (black), BPM-1st (blue) and BPM-2nd (red), (c) Raman spectra generated using DFT (black), BPM-1st (blue) and BPM-2nd (red).

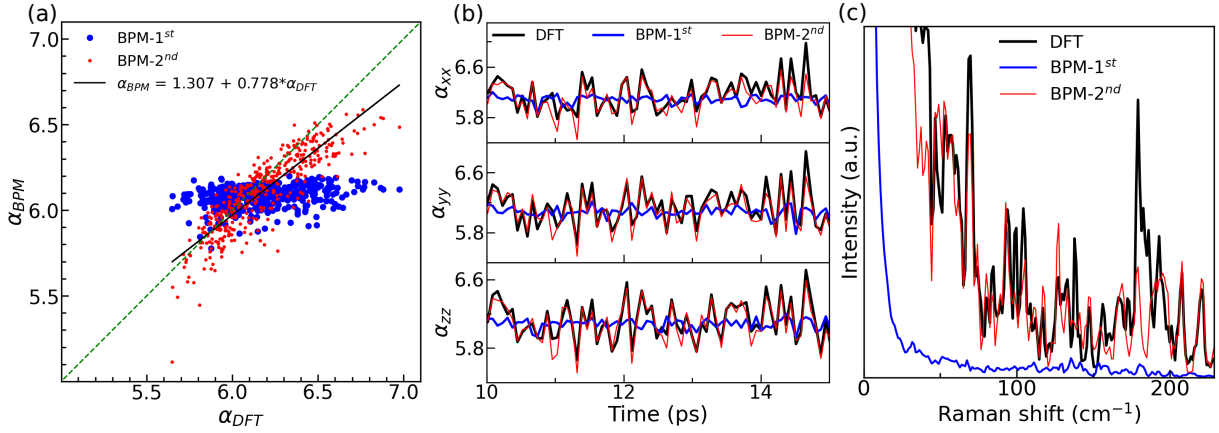


FIG. 12. (Color online) BaTiO₃ at 1000 K: (Color online) (a) The results for the xx component of α_{BPM} (1st and 2nd order BPM are shown by blue and red circles, respectively) plotted vs α_{DFT} . The linear fit of BPM-2nd order data is shown by the black line. The green dotted line represents $\alpha_{BPM} = \alpha_{DFT}$. (b) Comparison of the trajectory of α_{xx} (top panel), α_{yy} (middle panel) and α_{zz} (bottom panel) calculated from DFT (black), BPM-1st (blue) and BPM-2nd (red), (c) Raman spectra generated using DFT (black), BPM-1st (blue) and BPM-2nd (red).

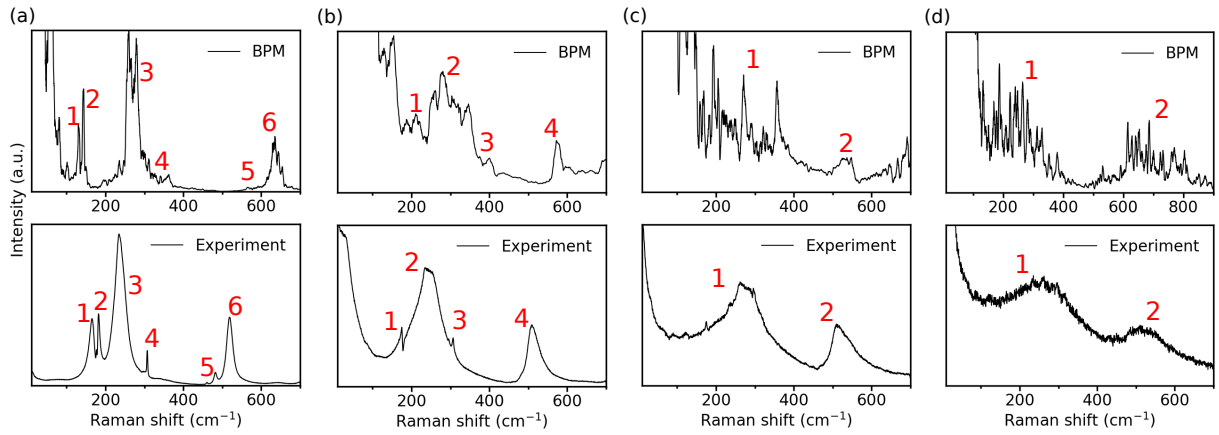


FIG. 13. (Color online) Raman spectra of different phases ((a) rhombohedral, (b) orthorhombic, (c) tetragonal, and (d) cubic) of BTO single crystal from bond polarizability model (top panel) and experiment (bottom panel). The temperatures for (a), (b), (c) and (d) are 60 K, 88 K, 110 K and 160 K, respectively (top panel), and 123 K, 233 K, 333 K, 423 K, respectively (bottom panel). Peaks from BPM and experiment are marked by number for comparison.

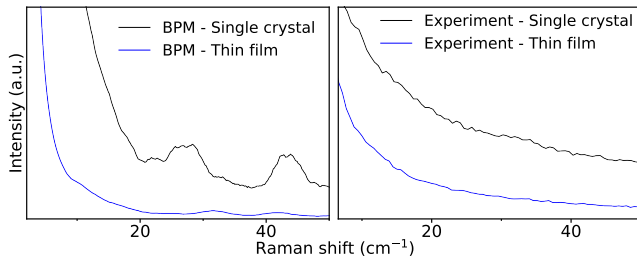


FIG. 14. (Color online) Central peak intensity of single crystal (black) and thin film (blue) of BTO (tetragonal phase) from BPM (left panel) and experiment (right panel). The temperature for left panel and right panel are 130 K and 333 K, respectively.

frequency region as shown in Fig. 12 (c). Interestingly, despite the stronger deviation of the BPM-2nd polarizabilities from DFT polarizability for 1000 K than 300 K, the Raman spectrum at 1000 K shows better agreement between DFT and BPM-2nd with only the peak at 180 cm⁻¹ showing strong underestimation of the intensity by BPM-2nd compared to DFT. This is likely either due to error cancellation or because the high errors of BPM-2nd are relevant for non-Raman-active modes that do not contribute to the error in the Raman spectrum. The lack of reliability of BPM-2nd for the peak intensity means that the temperature evolution of the Raman peaks is reproduced well for some peaks but is only qualitatively reproduced for other peaks. For example, DFT results for the ten-atom cell dynamics show that the intensity of the peak at 180 cm⁻¹ is weaker than that at 100 cm⁻¹ at 300 K and then increases with higher temperature so that at 1000 K the peak at 180 cm⁻¹ has much higher intensity than the peak at 100 cm⁻¹. By contrast, BPM-2nd spectra show that the peak at 180 cm⁻¹ changes from weaker intensity to same intensity as the peak at 100 cm⁻¹ when the temperature is changed from 300 to 1000 K. Thus, while the BPM qualitatively reproduces the overall trend of the changes in the relative intensities of the two peaks, it does not provide quantitative agreement with DFT.

The above BTO results are calculated for a large time step and a short trajectory because of the large computational cost of DFT-calculated polarizability. Therefore, to examine the performance of the BPM for obtaining Raman spectra of realistic model BTO, we performed classical molecular dynamics at different temperature for a longer trajectory of 220 ps and using the standard time step of 1 fs. The different phases of BTO were obtained by the classical molecular dynamics simulations at different temperatures, namely rhombohedral for $T < 80$ K, orthorhombic for $85 \text{ K} < T < 90$ K, tetragonal for $95 \text{ K} < T < 150$ K, and cubic for $155 \text{ K} < T$. These correspond to the experimentally observed phases of BTO, namely rhombohedral for $T < 183$ K, orthorhombic for $183 \text{ K} < T < 278$ K, tetragonal for $278 \text{ K} < T < 393$ K, and cubic for $393 \text{ K} < T$. As noted in previous studies, the lower temperatures of the simulated phase transitions compared to the experimental

values are due to fundamental inaccuracies of DFT calculations for BTO rather than due to the deficiency of the atomistic model²⁷. The BPM parameters determined to reproduce the polarizabilities of 10-atom BTO were used to calculate the polarizability trajectories for all phases. While in this case disagreement between theory and experiment may be due to both the errors in the polarizability calculations as well as the errors due to the atomistic potential, comparison of MD-derived and experimental Raman spectra will still reveal the usefulness of the atomistic MD + BPM approach for modeling and understanding of experimental Raman spectra.

Figs. 13 (a), (b), (c) and (d) compare the calculated BPM Raman spectra and experimental spectra for the rhombohedral, orthorhombic, tetragonal and cubic phases of BTO, respectively, in the 0-700 cm⁻¹ range. Examination of the figures shows that the BVMD-BPM spectra qualitatively reproduce the experimental peaks and their changes with temperature. The additional peak above 700 cm⁻¹ of the experimental range is also reproduced by BPM for the rhombohedral, orthorhombic and tetragonal phase (see SM). However, differences in the peak positions are observed for the BVMD-BPM peaks at lower frequencies in some cases (e.g. peaks 1 and 2 for R-phase, and peak 1 of the C-phase), and at higher frequencies in other cases (e.g. peaks 3-6 for R-phase and peaks 1-4 for the O phase). Considering that BPM reproduces the peak position of DFT spectra, as discussed above, it is likely that these differences are due to the error introduced by the use of the atomistic potential. Furthermore, the lineshapes and intensities of the peaks show differences for all phases, with particularly significant differences observed for the C-phase and T-phase peaks 1 and 2, and O-phase peak 2. This is consistent with the above-discussed errors induced in the peak intensity and lineshape by the errors in the polarizability trajectory.

To further examine the usefulness of the BVMD-BPM approach for BTO simulations, we compared experimental central peak spectra for bulk BTO and a thin BTO film clamped to the substrate (Fig. 14) to the BVMD-BPM spectra obtained from MD simulations of bulk BTO and a BTO supercell clamped in the x and y directions (i.e. fixed x - and y - lattice parameters while the z -axis lattice parameter is left free to vary), thus simulating the clamping of the film by the substrate. The BVMD simulations are performed at 130 K. At this temperature, BVMD simulations obtain the tetragonal phase of BTO corresponding to the experimentally observed tetragonal phase at room temperature.

Fig. 14 (left panel) shows that the central peak intensity as calculated from BPM is decreased for the thin-film structure in comparison to bulk structure, in agreement with the central peak intensity change observed experimentally. This indicates that the change in the central peak intensity is due to the clamping of the film by the substrate, rather than by nanoscale effects or domain walls, because neither domain walls nor free surfaces are present in the BVMD simulations. Taken together with the results presented in Figs. 13 and 14, these results show that BPM can be used for qualitative modeling of the BTO Raman spectra and their interpretation. However, fine features of the spectrum cannot be reproduced with the BPM. Next, we considered the CPB perovskite, which due to its soft

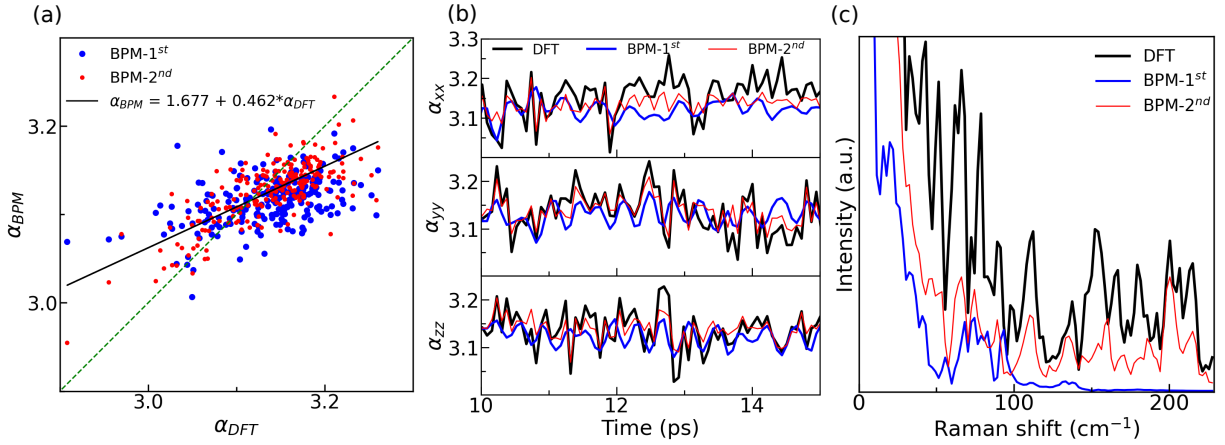


FIG. 15. (Color online) CsPbBr₃ at 300 K: (Color online) (a) The results for the xx component of α_{BPM} (1st and 2nd order BPM are shown by blue and red circles, respectively) plotted vs α_{DFT} . The linear fit of BPM-2nd order data is shown by the black line. The green dotted line represents $\alpha_{BPM} = \alpha_{DFT}$. (b) Comparison of the trajectory of α_{xx} (top panel), α_{yy} (middle panel) and α_{zz} (bottom panel) calculated from DFT (black), BPM-1st (blue) and BPM-2nd (red), (c) Raman spectra generated using DFT (black), BPM-1st (blue) and BPM-2nd (red).

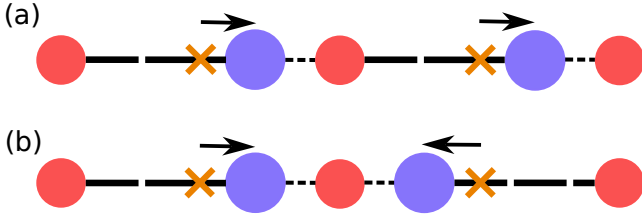


FIG. 16. (Color online) In a one-dimensional chain of O-Ti-O-Ti-O, (a) head-to-tail, (b) head-to-head, movement of dipole formed due to the displacement of Ti from the center of O as marked by yellow cross. Red and blue circles corresponding to O and Ti, respectively. Each arrow indicate the movement of the dipole.

bonds and large distortions at even relatively low temperature poses a challenge for atomistic polarizability modeling. Fig. 15 (a) compares the BPM-calculated polarizability with the DFT-calculated polarizability of CPB at 300 K. It can be seen that a high scatter that is much stronger than that for BTO is observed even for the BPM-2nd data. Similarly, the polarizability trajectories show stronger deviations of the BPM-2nd results from the DFT results compared to BTO. Comparison of the DFT and BPM-2nd Raman spectra shows that even in this case, BPM-2nd results match the peak position of the DFT data. However, the agreement between the relative intensities is quite poor.

Consideration of the perovskite structures and the possible distortions shows that there are several sources of error in the BPM for the modeling of BTO, CPB and other perovskites. The most basic shortcoming is that the strong distortions in these systems may require higher-order terms in the Taylor expansion of bond polarizability to reproduce the DFT results. However, results obtained 3rd- and 4th-order BP models for BTO show only a slight improvement in agreement with DFT results (see SM). Second, similar to the molecular systems, the independent bond approximation of the BPM ignores the

effect of Ti-O-Ti and O-Ti-O (Pb-Br-Pb and Br-Pb-Br) angle changes in BTO (CPB). Third, due to its dependence on the bond lengths only, the BPM cannot distinguish between the head-to-head and head-to-tail dipole structures created by the displacements of the B-cations from the centers of their octahedra, as illustrated in Fig. 16. The second and third effects cannot be addressed in the BPM framework due to its fundamental assumption of non-interacting independent contributions of each bond to the total polarizability. In fact, these effects are the primary origin of the disagreement between the DFT and BPM polarizability results for BTO and CPB as demonstrated by the weak improvement provided by the BPM-3rd and BPM-4th models for BTO (see SM). Thus, the BPM must be fundamentally modified to include the interactions between bonds to achieve accurate prediction of polarizability for solid-state perovskite systems.

IV. CONCLUSIONS

We have investigated the applicability of the bond polarizability model to the modeling of polarizability and Raman spectra using trajectories obtained from MD simulations. We find that BPM including second-order terms generally gives qualitative agreement with the DFT results such that the positions of the Raman peaks are reproduced accurately but their intensities can differ from those obtained by quantum-mechanical calculations. Structures with higher symmetry and with angular vibrations for which the polarizability changes are second-order in the angle change (e.g. CH₄) show much higher accuracy than highly asymmetric molecules (most importantly water) for which the effect of angle changes on the polarizability is linear in the angle change. Similarly, BPM accuracy is much higher for molecules with stiff angular potential energy surface due to sp^2 bonding (e.g. CH₂O and thiophene). For solid-state BTO perovskite, qualitative accuracy is obtained for the BPM-2nd model while for

the much softer and distorted CPB, BPM shows poor agreement. Due to its simplicity, BPM provides a good starting point for simulations of Raman spectra and can be relied upon to reproduce and interpret strong changes in the experimental Raman spectra. However, the shortcomings of the BPM due to the assumption of non-interacting bonds make it incapable of obtaining quantitative accuracy except for highly symmetric systems and lead to complete failure in case of systems where large deviations from the ground state structure are present. Thus, to enable reliable interpretation of fine features of Raman spectra, it is necessary to develop atomistic models for polarizability that can include the effects of interactions between bonds and angles.

ACKNOWLEDGMENTS

A.P., A.R., S. M., J.E.S. and I.G. acknowledge the support of the Army Research Office under Grant W911NF-21-1-0126 and Army/ARL via the Collaborative for Hierarchical Agile and Responsive Materials (CHARM) under cooperative agreement W911NF-19-2-0119. A.P. and I.G. acknowledge additional support from Israel Science Foundation under Grant 1479/21.

DATA AVAILABILITY

The data used in this work are available from the corresponding author upon reasonable request.

- ¹A. Orlando, F. Franceschini, C. Muscas, S. Pidkova, M. Bartoli, M. Rovere, and A. Tagliaferro, *Chemosensors* **9**, 262 (2021).
- ²D. A. Long, *The Raman Effect* (John Wiley & Sons, Ltd, 2002).
- ³M. Gastegger, J. Behler, and P. Marquetand, *Chem. Sci.* **8**, 6924 (2017).
- ⁴M.-P. Gaigeot and M. Sprik, *The Journal of Physical Chemistry B* **107**, 10344 (2003).
- ⁵M. Thomas, M. Brehm, R. Fligg, P. Vöhringer, and B. Kirchner, *Phys. Chem. Chem. Phys.* **15**, 6608 (2013).
- ⁶A. Putrino and M. Parrinello, *Phys. Rev. Lett.* **88**, 176401 (2002).
- ⁷S. Lubber, M. Iannuzzi, and J. Hutter, *The Journal of Chemical Physics* **141**, 094503 (2014).
- ⁸J. Mattiat and S. Lubber, *Journal of Chemical Theory and Computation* **17**, 344 (2021).
- ⁹M. Lazzeri and F. Mauri, *Phys. Rev. Lett.* **90**, 036401 (2003).
- ¹⁰F. Lussier, V. Thibault, B. Charron, G. Q. Wallace, and J.-F. Masson, *TrAC Trends in Analytical Chemistry* **124**, 115796 (2020).
- ¹¹G. M. Sommers, M. F. Calegari Andrade, L. Zhang, H. Wang, and R. Car, *Phys. Chem. Chem. Phys.* **22**, 10592 (2020).
- ¹²E. Berger, J. Niemelä, O. Lampela, A. H. Juffer, and H.-P. Komsa, "Raman spectra of amino acids and peptides from machine learning polarizabilities." (2024), [arXiv:2401.14808 \[physics.comp-ph\]](https://arxiv.org/abs/2401.14808).
- ¹³N. Raimbault, A. Grisafi, M. Ceriotti, and M. Rossi, *New Journal of Physics* **21**, 105001 (2019).
- ¹⁴S. Montero and G. del Rio, *Molecular Physics* **31**, 357 (1976).
- ¹⁵M. Cardona, R. Chang, G. Güntherodt, M. Long, and H. Vogt, *Light Scattering in Solids II: Basic Concepts and Instrumentation*, Topics in Applied Physics (Springer-Verlag Berlin Heidelberg 1982).
- ¹⁶in *Vibrational Intensities*, Vibrational Spectra and Structure, Vol. 22, edited by B. S. Galabov and T. Dudev (Elsevier, 1996) pp. 215–271.
- ¹⁷L. Liang, A. A. Puretzy, B. G. Sumpter, and V. Meunier, *Nanoscale* **9**, 15340 (2017).
- ¹⁸L. Wirtz, M. Lazzeri, F. Mauri, and A. Rubio, *Phys. Rev. B* **71**, 241402 (2005).
- ¹⁹X. Luo, X. Lu, C. Cong, T. Yu, Q. Xiong, and S. Ying Quek, *Scientific Reports* **5**, 14565 (2015).
- ²⁰P. Umari, A. Pasquarello, and A. Dal Corso, *Phys. Rev. B* **63**, 094305 (2001).
- ²¹P. Hermet, N. Izard, A. Rahmani, and P. Ghosez, *The Journal of Physical Chemistry B* **110**, 24869 (2006).
- ²²E. Berger and H.-P. Komsa, "Polarizability models for simulations of finite temperature raman spectra from machine learning molecular dynamics." (2023), [arXiv:2310.13310 \[cond-mat.mes-hall\]](https://arxiv.org/abs/2310.13310).
- ²³S. Baroni, S. de Gironcoli, A. Dal Corso, and P. Giannozzi, *Rev. Mod. Phys.* **73**, 515 (2001).
- ²⁴P. Giannozzi, S. Baroni, N. Bonini, M. Calandra, R. Car, C. Cavazzoni, D. Ceresoli, G. L. Chiarotti, M. Cococcioni, I. Dabo, A. D. Corso, S. de Gironcoli, S. Fabris, G. Fratesi, R. Gebauer, U. Gerstmann, C. Gougoussis, A. Kokalj, M. Lazzeri, L. Martin-Samos, N. Marzari, F. Mauri, R. Mazzarello, S. Paolini, A. Pasquarello, L. Paulatto, C. Sbraccia, S. Scandolo, G. Sclauzero, A. P. Seitsonen, A. Smogunov, P. Umari, and R. M. Wentzcovitch, *Journal of Physics: Condensed Matter* **21**, 395502 (2009).
- ²⁵J. P. Perdew, A. Ruzsinszky, G. I. Csonka, O. A. Vydrov, G. E. Scuseria, L. A. Constantin, X. Zhou, and K. Burke, *Phys. Rev. Lett.* **100**, 136406 (2008).
- ²⁶A. P. Thompson, H. M. Aktulga, R. Berger, D. S. Bolintineanu, W. M. Brown, P. S. Crozier, P. J. in 't Veld, A. Kohlmeyer, S. G. Moore, T. D. Nguyen, R. Shan, M. J. Stevens, J. Tranchida, C. Trott, and S. J. Plimpton, *Comp. Phys. Comm.* **271**, 108171 (2022).
- ²⁷Y. Qi, S. Liu, I. Grinberg, and A. M. Rappe, *Phys. Rev. B* **94**, 134308 (2016).
- ²⁸M. Deluca, Z. G. Al-Jlaihawi, K. Reichmann, A. M. T. Bell, and A. Feteira, *J. Mater. Chem. A* **6**, 5443 (2018).
- ²⁹Y. I. Yuzyuk, *Physics of the Solid State* **54**, 1026 (2012).

Supplementary Material for Accuracy and limitations of the bond polarizability model in modeling of Raman spectra from molecular dynamics simulations

Atanu Paul,¹ Maya Rubenstein,¹ Anthony Ruffino,² Stefan Masiuk,³ Jonathan Spanier,^{3,2} and Ilya Grinberg¹

¹Department of Chemistry, Bar-Ilan University, Ramat Gan 5290002, Israel

²Department of Physics, Drexel University, Philadelphia, Pennsylvania 19104, USA

³Department of Materials Science and Engineering, Drexel University, Philadelphia, Pennsylvania 19104, USA

(*ilya.grinberg@biu.ac.il)

I. EFFECT OF BaO_{12} ON POLARIZABILITY OF BaTiO_3

In order to understand the effect of BaO_{12} on the polarizability of BaTiO_3 (BTO), we have considered a cubic 5-atom unit cell of BTO and calculated polarizability from DFT for different displacements of Ba and Ti atoms along the [100] direction from their high-symmetry positions. Fig. S1 (a) shows the DFT-calculated α_{xx} and α_{yy} as a function of Ti displacement (d_{Ti} , d_{Ti} is the displacement of the Ti atom from its centrosymmetric position) for two Ba positions ($d_{Ba} = 0.00$ and 0.08 Å, where d_{Ba} is the displacement of the Ba atom from its centrosymmetric position). The results show a nearly parabolic dependence of α_{xx} and α_{yy} for the displacement of Ti. By contrast, the results for the two different Ba positions ($d_{Ba} = 0.00$ and 0.08 Å) show nearly identical α_{xx} and α_{yy} values. This implies that the polarizability of BTO is mostly controlled by the Ti and O movement, and the movement of Ba has only a weak effect on the polarizability. In Fig. S1 (b), we show the dependence of α_{xx} and α_{yy} as a function of Ba displacement for two different Ti positions ($d_{Ti} = 0.00$ and 0.08 Å). As expected, only weak changes in the polarizability values are obtained for Ba displacements. The above observations are due to the fact that Ti atoms are strongly covalently bonded with the O atoms, whereas the bonds between O and Ba atoms are mostly ionic. Therefore, for simplicity, we have neglected the effect of BaO_{12} bonds in our bond polarizability model for BTO.

II. EFFECT OF CsBr_{12} ON POLARIZABILITY OF CsPbBr_3

We followed the procedure described above for BTO in order to understand the effect of CsBr_{12} complex on the polarizability of CsPbBr_3 (CPB). We considered 5-atom cell of CPB and displaced Cs and Pb atoms along the [111] direction from their high-symmetry positions. In Fig. S2 (a), we show the dependence of α_{xx} on Pb-displacement from its centrosymmetric position denoted by d_{Pb} for three different Cs positions ($d_{Cs} = 0.00, 0.41$ and 0.81 Å, where d_{Cs} be the displacement of the Cs atom from its centrosymmetric position). Similar to BTO, α_{xx} shows a strong dependence on the value of d_{Pb} irrespective of the value of d_{Cs} . This indicates that PbBr_6 strongly

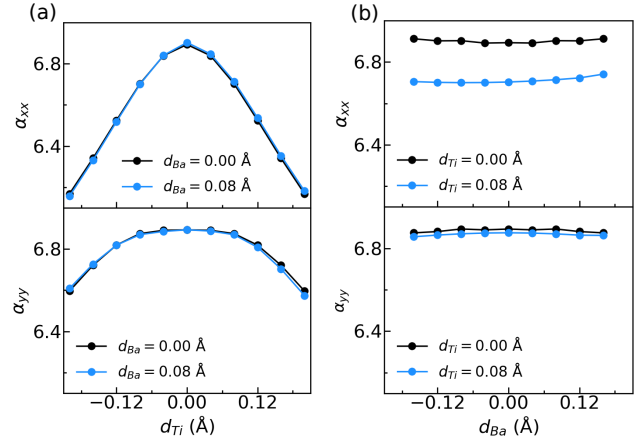


FIG. 1. (Color online) α_{xx} and α_{yy} of BTO (5-atom cell) calculated from DFT, where d_{Ba} and d_{Ti} are the displacements of Ba and Ti atoms, respectively, along the [100] direction from their high-symmetry positions denoted by $d_{Ba} = 0$ and $d_{Ti} = 0$. (a) α_{xx} (top panel) and α_{yy} (bottom panel) as a function of d_{Ti} for two values of d_{Ba} (0.00 and 0.08 Å). (b) α_{xx} (top panel) and α_{yy} (bottom panel) as a function of d_{Ba} for two values of d_{Ti} (0.00 and 0.08 Å).

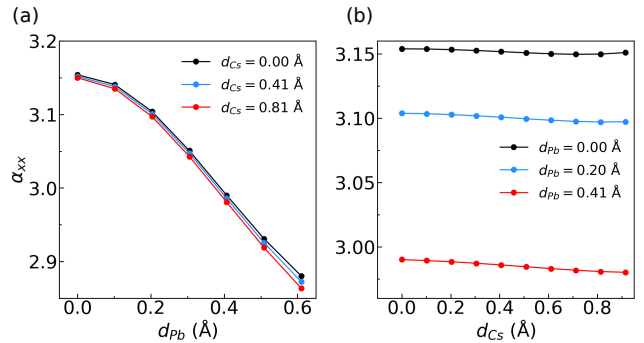


FIG. 2. (Color online) α_{xx} of CPB (5-atom cell) calculated from DFT, where d_{Cs} and d_{Pb} are the displacements of Cs and Pb atoms, respectively, along the [111] direction from their high-symmetry positions denoted by $d_{Cs} = 0$ and $d_{Pb} = 0$. (a) α_{xx} as a function of d_{Pb} for three values of d_{Cs} (0.00, 0.41 and 0.81 Å). (b) α_{xx} as a function of d_{Cs} for three values of d_{Pb} (0.00, 0.20 and 0.41 Å).

controls the value of the polarizability in CPB with only weak

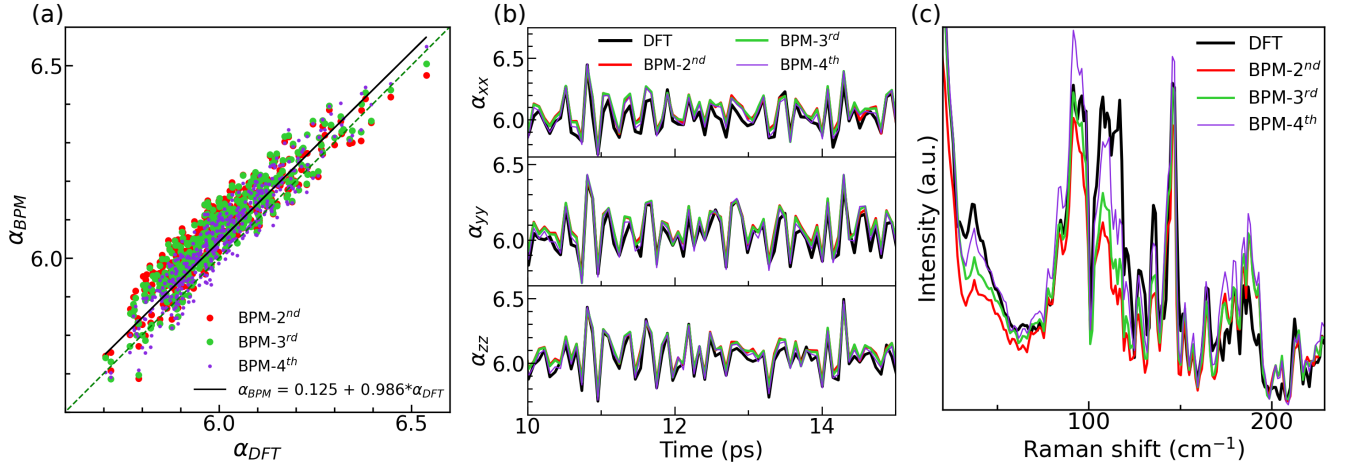


FIG. 3. (Color online) BaTiO₃ at 300 K: (Color online) (a) The results for the xx component of α_{BPM} (2nd, 3rd and 4th order BPM are shown by red, green and violet circles, respectively) plotted vs α_{DFT} . The linear fit of BPM-4th order data is shown by the black line. The green dotted line represents $\alpha_{BPM} = \alpha_{DFT}$. (b) Comparison of the trajectory of α_{xx} (top panel), α_{yy} (middle panel) and α_{zz} (bottom panel) calculated from DFT (black), BPM-2nd (red), BPM-3rd (green) and BPM-4th (violet) order. (c) Raman spectra generated using DFT (black), BPM-2nd (red), BPM-3rd (green) and BPM-4th (violet).

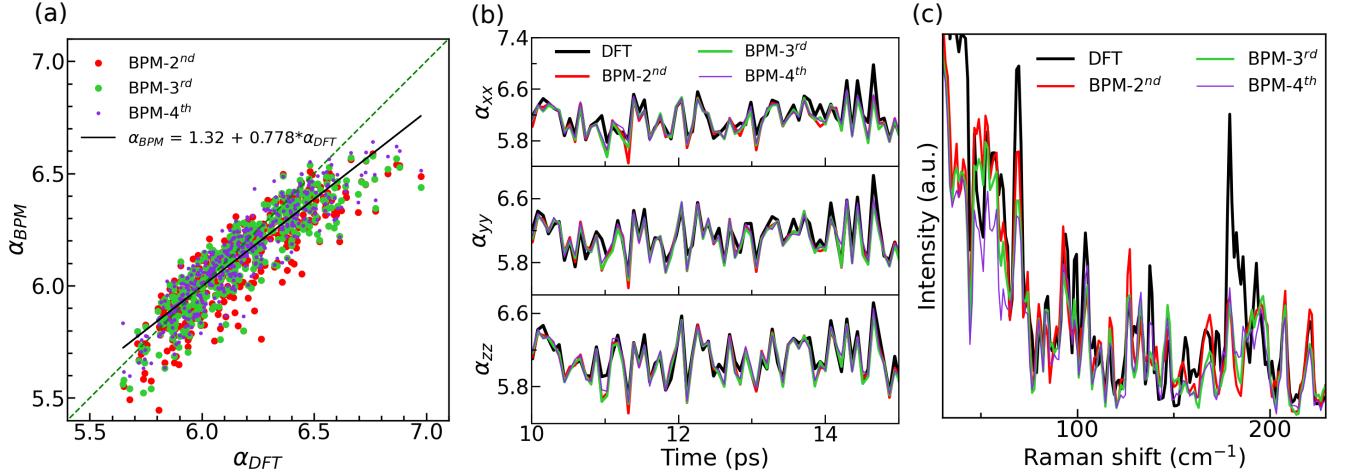


FIG. 4. (Color online) BaTiO₃ at 1000 K: (Color online) (a) The results for the xx component of α_{BPM} (2nd, 3rd and 4th order BPM are shown by red, green and violet circles, respectively) plotted vs α_{DFT} . The linear fit of BPM-4th order data is shown by the black line. The green dotted line represents $\alpha_{BPM} = \alpha_{DFT}$. (b) Comparison of the trajectory of α_{xx} (top panel), α_{yy} (middle panel) and α_{zz} (bottom panel) calculated from DFT (black), BPM-2nd (red), BPM-3rd (green) and BPM-4th (violet) order. (c) Raman spectra generated using DFT (black), BPM-2nd (red), BPM-3rd (green) and BPM-4th (violet).

effect of CsBr₁₂ on the polarizability. This is further seen in the Fig. S2 (b), where α_{xx} hardly shows any changes with the Cs displacement (d_{Cs}) for the three Pb positions ($d_{Pb} = 0.00, 0.20$ and 0.41 Å). Therefore, we neglected the effect of Cs in the calculation of the polarizability of CPB using BPM.

III. BPM-3rd AND BPM-4th OF BATIO₃ AT 300 K AND 1000 K

Fig. S3 (a) presents the plots of α_{xx} as calculated using BPM-3rd and BPM-4th versus the DFT-calculated α_{xx} for 10-atom BTO along the polarizability trajectory at 300 K.

For better understanding of the effect of the inclusion of the higher-order-BPM, we have also shown the results of BPM-2nd in the same plot. A clear improvement in the results is observed from BPM-2nd to BPM-3rd to BPM-4th with the value of the slope of the linear fit for BPM-4th (0.986) order data improved compared to BPM-2nd (0.866) order data. However, the linear-fitted line for BPM-4th is far from the exact $\alpha_{BPM} = \alpha_{DFT}$ line (see Fig. S3 (a)). We then compare the calculated time-dependent polarizability trajectory of BPM-2nd, BPM-3rd and BPM-4th with DFT in Fig. S3 (b). Though the BPM-4th-order shows better results, comparison to DFT results shows that the BPM-4th-order still does not correct the several deviations from the DFT polarizabil-

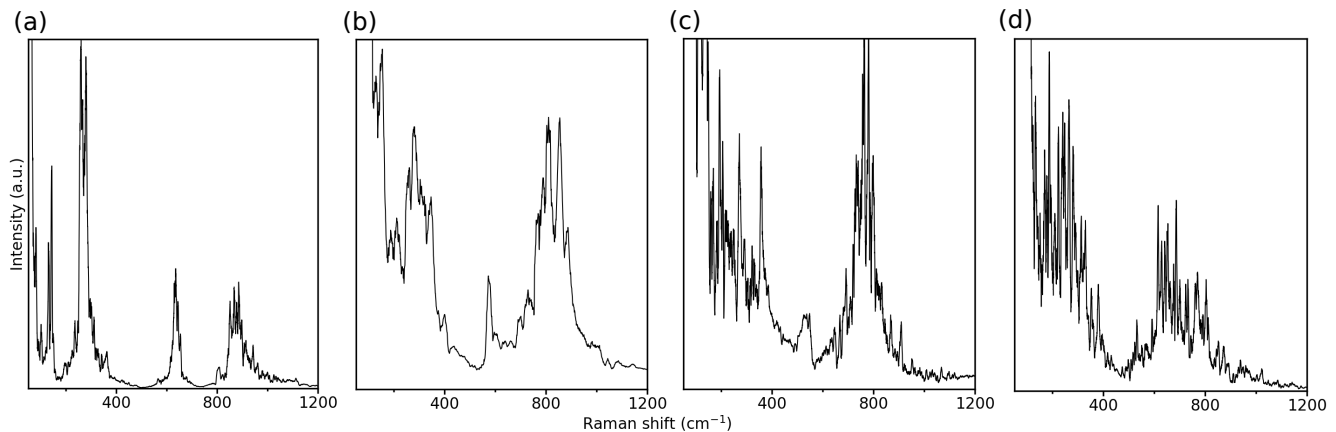


FIG. 5. (Color online) Raman spectra of different phases ((a) rhombohedral, (b) orthorhombic), (c) tetragonal, and (d) cubic) of BTO single crystal from bond polarizability model (2^{nd} order). The temperatures for (a), (b), (c) and (d) are 60 K, 88 K, 110 K and 160 K, respectively.

ity trend obtained by BPM- 2^{nd} (e.g. see α_{zz} at 13 ps). This mismatch of DFT and BPM results is also reflected in the Raman spectra. The Raman spectra calculated with BP models of different orders are shown along with the DFT spectrum in Fig. S3 (c). The peak position of the DFT spectrum is well reproduced by the BPM (2^{nd} , 3^{rd} and 4^{th}). However, the DFT-calculated peak intensities are not captured well by the BPM (2^{nd} , 3^{rd} and 4^{th}).

We also compare the results of BPM- 3^{rd} and BPM- 4^{th} with DFT results for BTO at 1000 K to check whether the higher order of BPM can improve the accuracy of the BPM results. Fig. S4 (a) shows the results of BPM- 2^{nd} , BPM- 3^{rd} and BPM- 4^{th} plotted DFT values. Even though the results are improved overall with the inclusion of higher order of BPM, the improvement in the accuracy from BPM- 2^{nd} to BPM- 3^{rd} to

BPM- 4^{th} is not as significant as that obtained for the 300 K results. This can be seen from the values of the calculated slope of the linearly fitted data points of BPM- 2^{nd} (0.778) and BPM- 4^{th} (0.778) which are the same. The comparison of time-dependent polarizability trajectory (Fig. S4 (b)) from different order of BPM and the corresponding Raman spectra (Fig. S4 (c)) also show a noticeable disagreement with the DFT results.

IV. RAMAN SPECTRA OF BATiO_3 SINGLE CRYSTAL

The Raman spectra of single crystal BTO for all phases using BPM- 2^{nd} are shown in Fig. S5.